



Full length article

Defect accumulation and evolution in refractory multi-principal element alloys



Shijun Zhao*, Yaoxu Xiong, Shihua Ma, Jun Zhang, Biao Xu, Ji-Jung Kai

Department of Mechanical Engineering, City University of Hong Kong, Hong Kong

ARTICLE INFO

Article history:

Received 17 May 2021

Revised 6 July 2021

Accepted 7 August 2021

Available online 13 August 2021

Keywords:

Multiple principal elemental alloys

Defect accumulation

Defect evolution

Molecular dynamics

Diffusion

ABSTRACT

Refractory multiple principal elemental alloys (MPEAs) hold great promise for structural materials in future nuclear energy systems. Compared to the extensively studied face-centered cubic (FCC) MPEAs, the irradiation resistance of body-centered cubic (BCC) refractory MPEAs is relatively less known. In this work, we study defect accumulation and evolution in two BCC VTaTi and VTaW MPEAs comparatively through atomistic simulations. For this purpose, we have parameterized the Embedded Atom Method (EAM) potential parameters for V metals. Combined with available potential parameters for other elements, we construct average atom models for the considered alloys to elucidate the effects of chemical complexities in BCC MPEAs. Our results based on Frenkel pair accumulation simulations suggest that the major influence of chemical fluctuations in BCC MPEAs is on the clustering behavior of defects, which leads to discrete point defects or small defect clusters, in contrast to the large defect clusters observed in the average atom model. We further show that the diffusion of interstitial clusters exhibits different modes due to chemical complexity. While interstitials show either three-dimensional or one-dimensional diffusion in the average atom model, the mean free path of interstitials in the random alloy is strongly suppressed. These results provide fundamental insights into the irradiation response of BCC MPEAs and pinpoint the critical role of chemical complexity on defect evolution, which lay the basis for the future development of irradiation-resistant structural materials based on BCC MPEAs.

© 2021 Acta Materialia Inc. Published by Elsevier Ltd. All rights reserved.

1. Introduction

Nuclear energy is one of the most promising ways to solve the energy crisis in the world. For better safety and economics, the concept of advanced generation-IV reactors has been proposed [1]. In these advanced nuclear systems, structural materials need to endure harsh environments, including high temperature, corrosion, and irradiations [2]. New materials that can fulfill these requirements are urgently needed for the deployment of generation-IV reactors. As a novel class of alloys, high-entropy alloys (HEAs), also called multi-principal elemental alloys (MPEAs), represent a new strategy for alloy design [3–5]. In contrast to traditional alloys usually containing one or two major elements, MPEAs comprise multiple principal elements, all at high concentrations [6]. Due to the high concentration of different species in the lattice, MPEAs are characterized by extreme chemical disorder and site-to-site lattice distortion, leading to their outstanding mechanical properties and irradiation resistance [7–11].

Most previous studies on irradiation response of MPEAs are focused on model alloy systems with face-centered cubic (FCC) structures, specifically, the Cantor alloy (CoCrFeNiMn) and its derived subsystems [5,7,12–14]. These alloys are ideal systems for fundamental research on the governing mechanism of irradiation resistance of MPEAs, since all the derived alloys from the Cantor alloy also can form single-phase concentrated alloys. Hence, it is possible to tune elemental species one at a time to reveal the role of individual elements on the irradiation performance. Nevertheless, this series of alloys is not suitable for future nuclear applications as it contains neutron activation elements, such as Co. Efforts have been devoted to developing Co-free MPEAs based on FCC structures, such as CrFeNiMn [15,16].

Compared to FCC MPEAs, refractory MPEAs consisting of group V and VI transition metals with body-centered cubic (BCC) structures provide a feasible way to design structural materials for advanced nuclear reactors. As the elements in the refractory MPEAs generally possess high melting points and good mechanical strength, this type of MPEAs is promising for high-temperature nuclear applications. Available reports on irradiation response of refractory MPEAs show that these alloys exhibit high irradiation tolerance, with little radiation hardening and no signs of radiation-

* Corresponding author:

E-mail address: shijzhao@cityu.edu.hk (S. Zhao).

induced dislocation loops even at high irradiation doses [17–20]. Combining with their excellent high-temperature mechanical properties, the refractory MPEAs are potential candidate materials for future nuclear systems where high temperature, corrosion, and irradiation conditions exist.

It is well established that the irradiation damage mechanism of BCC materials is fundamentally different from FCC ones in many aspects [21,22]. For example, void swelling, which is a major concern in materials under irradiation at high-temperature conditions, is significantly lower in BCC materials compared to FCC ones generally. Because of the high stacking fault energy, sessile faulted dislocation loop formation is energetically unfavorable in most BCC materials. Instead, glissile perfect $\frac{1}{2}\langle 111 \rangle$ loops are preferred. Even for the primary damage states, it is found that the fraction of defects in clusters is lower in BCC materials than in FCC ones [23]. In principle, the different defect properties in BCC materials from FCC ones arise from their loose-packed crystal structures. Though defect energetics and defect migration mechanisms in FCC MPEAs have been studied in-depth [8,9,12–14,24,25], relatively less is known for MPEAs with BCC structures. In particular, how chemical disorder in BCC MPEAs affects defect accumulation and evolution is not clear.

Another peculiarity of BCC MPEAs is the significant local lattice distortion, which helps stabilize the structure and affect their multiple properties [26]. Direct comparisons between HEAs with FCC and BCC structures show different deformation modes and temperature dependence of mechanical properties pertaining to their differences in dislocation activities and slip systems [11,27,28]. Regarding defect properties under irradiation, previous density-functional theory (DFT) calculations indicate that due to the significant lattice distortion, defect formation and migration energies in BCC MPEAs exhibit broad distributions, inducing highly heterogeneous defect diffusion [29]. Besides, interstitials may appear in different orientations compared to pure BCC metals, which can further influence their migration mechanisms [29]. Some experimental studies on BCC MPEAs [20,30,31] demonstrate outstanding irradiation resistance with almost no dislocation loops, dictating their peculiar defect accumulation and evolution properties.

In this work, we compare the irradiation response of two refractory MPEAs, VTaTi and VTaW, through atomistic simulations. These MPEAs are the composition unit of complexed TaVCrW and TaTiV(Zr,Hf) HEAs with low neutron activation, which possess good mechanical strength and irradiation tolerance [20,30]. More importantly, VTaTi has been shown to have good thermal stability and irradiation performance recently [32]. We first parameterized an empirical potential for the V metal, which enables us to model the considered alloys. To reveal the effects of chemical fluctuations and local lattice distortion, we construct an average atom potential and compare the results between the random alloy and the average model. Our results reveal that chemical complexities in BCC MPEAs play decisive roles in influencing defect accumulation and evolution properties.

2. Method

Simulations were performed using the large-scale atomic/molecular massively parallel simulator (LAMMPS) [33]. Interatomic interactions were described based on the embedded atom method (EAM) parameterized by Zhou et al. [34] for the Ta, Ti, W elements. For V, we fitted the EAM parameters based on the formalism of Zhou et al., which allows us to have a unified description of the considered MPEAs. Precisely, the pair potential between any two different elements is analytically calculated by virtue of the density functions of pure elements [34]. The complete EAM formulae and optimized parameters are provided in the Appendix. To reveal the effects of chemical complexity in MPEAs,

we also performed simulations using the average atom potential constructed from the true alloy potential [35]. The average atom potential represents the average properties of the random alloy, resulting in a consistent description of the lattice constant, elastic constants, etc., as listed in the Appendix. Nonetheless, chemical fluctuations are not included in the average atom model. The comparison of the random alloy and the average atom model can then be used to elucidate the effects of chemical complexities, e.g., fluctuations in chemical occupancy, local lattice distortions, and atomic relaxations.

Defect accumulation simulations were performed by the Frenkel pair accumulation (FPA) method within a $42 \times 42 \times 42$ BCC supercell containing 148,176 atoms. Periodic boundary conditions were applied in all three directions. The system was first allowed to relax at given temperatures within an NPT ensemble for 100 ps with a timestep of 1 fs. Afterward, a randomly chosen atom was displaced at a separation of 5 Å in a random direction. The system was then allowed to relax in an NVE ensemble for 10 ps, followed by an NPT run for another 10 ps. These successive runs help relax the pressure to zero and the temperature to the target temperature. The simulations were carried out at two temperatures, namely 300 and 1000 K. As discussed in previous works [36], due to the short relaxation time after the introduction of a Frenkel pair, the FPA simulation is more consistent with low-temperature cases where long-range diffusion is not significant. The results from FPA can reflect the defect recombination and accumulation properties, and it can also provide information on stable defects. The final structures were visualized through the Wigner-Seitz (WS) defect analysis, as implemented in the Ovito software [37].

To further understand defect evolution in the considered MPEAs, we have analyzed defect energetics and diffusion properties. These simulations were performed in a $20 \times 20 \times 20$ BCC supercell at different temperatures ranging from 500 to 1000 K. The defect formation energies were calculated by

$$E_f = E_d - E_p \pm n_d \mu_d, \quad (1)$$

where E_d and E_p are the energies of defective and perfect supercells respectively, and μ_d is the chemical potential of the removed (+) or added (-) elements in order to create n_d vacancies or interstitials. Here, the chemical potential was calculated as the energy per atom in the corresponding pure metals. The migration energy of defects was determined using the climbing-image nudged elastic band (CI-NEB) method [38] as implemented in LAMMPS with a time step of 0.01 fs and a total of 15 intermediate images. The force convergence criterion in NEB calculations was 1×10^{-6} eV/Å.

The diffusion of interstitial clusters containing 1 to 25 interstitials was simulated to understand the observed defect evolution. These simulations were carried out in an NPT ensemble with a timestep of 1 fs. The total simulation time is around 40 ns. During diffusion, defect positions were recorded every 40 fs, which allowed analyzing the defect diffusivity and correlation factors [39]. For point defect, the defect position is well defined as the WS cell position with the atomic occupation number not equal to 1. For defect clusters, defect position is measured by the center of mass (COM) position of all the WS cell positions containing defects [40]. The number of jumps of the single defect or defect clusters was then counted if the jump distance is equal to or larger than the first nearest neighbor (1nn) distance, $\frac{\sqrt{3}}{2} a_0$, where a_0 is the lattice constant.

With the obtained defect trajectory, defect diffusivity D_d was obtained by decomposing the trajectory into segments with equal jump numbers [40,41], which is defined as

$$D_d = \frac{1}{N_{sg}} \sum_i \frac{R_i^2}{2nt_{sg}}, \quad (2)$$

where N_{sg} is the number of segments of duration t_{sg} , R_i^2 is the squared displacement in the decomposed trajectory, and n is the dimensionality of defect motion. As discussed previously [40,41], the choice of N_{sg} should not be too large nor too small in order to get good statistics of D_d . In this work, the length of N_{sg} is around 60. In crystalline materials, defect motion can be described in terms of discrete jumps with the same jump distance Δ (i.e., 1nn distance $\frac{\sqrt{3}}{2}a_0$). Therefore, the defect diffusion coefficient D_v^d can be estimated as

$$D_v^d = f_c \frac{\Gamma \Delta^2}{2n}, \quad (3)$$

where f_c is the correlation factor of defect jumps calculated from jump directions, and Γ is the jump frequency. In this study, Γ was calculated by monitoring the time interval between successive defect jumps, as did in our previous study [42]. The temperature dependence of jump frequency obeys the Arrhenius law

$$\Gamma(T) = \Gamma_0 \exp\left(-\frac{E_m^*}{k_B T}\right), \quad (4)$$

where Γ_0 is the attempt frequency, and E_m^* is the migration energy from jump frequency, which may be different from the effective defect migration energies derived from the Arrhenius law for defect diffusivity [43].

3. Result

3.1. EAM potential for V

Molecular simulations on MPEAs usually involve multiple metallic elements, which pose grand challenges to model their interactions within the same theoretical frame. In previous studies, Zhou et al. developed an integrated EAM potential database applicable to a number of metals and their alloys [34]. Due to its simplicity and consistency among different elements, this set of EAM parameters have been extensively used to simulate the properties of MPEAs [44–47]. In this potential, the parameters for the alloy phase can be constructed from elemental EAM parameters after normalization [34]. In the published literature, there are EAM parameters for most metallic elements, but not for V. Therefore, in this study, we first develop EAM parameters for V based on the EAM formalism described in [34].

We use the unconstrained minimization method to fit the V potential. The target values are lattice constant (a_0), cohesive energies (E_c), vacancy formation energies (E_f), elastic constants (C_{11} , C_{12} , and C_{44}), and the bulk modulus (B). The objective function is thus weighted squared deviation of the obtained properties from their target values,

$$f = \sum_i w_i (v_{\text{potential}} - v_t)^2, \quad (5)$$

where w_i is the weight to reconcile orders of magnitude differences in the considered target values (e.g., a_0 and B), $v_{\text{potential}}$ is the value obtained from the potential, and v_t is the target value.

The fitted potential parameters are provided in the Appendix. The performance of the developed potential is shown in Table 1, comparing with available data from density-functional theory (DFT) calculations [48] and existing empirical V potentials [48,49]. Besides the target values included in the fitting process, it can be seen that our developed potential provides a good overall description of the properties of V, especially for the structural properties. For defect-related properties, the potential slightly underestimates surface energies compared to DFT results, though the relative stability is correctly reproduced. Based on the developed V potential, we employ the mixing rules to construct alloy potentials to study defect accumulation and evolution in VTiTa and VTaW. The results

in both alloys are further compared with the average atom potential [35] built for each alloy. The properties of MPEAs predicted by the constructed potentials are provided in the Appendix. It is demonstrated that the lattice constants from our potential are in good agreement with previous DFT [50] and experiment [32] results, providing further validation of the present potential.

3.2. Defect accumulation

The calculated defect number as a function of the number of FP introduction events based on our FPA simulations is shown in Fig. 1. The defect number increases linearly with the number of FP events initially. Defect recombination comes into play with further increasing FP events, leading to a saturation of defect number in the system. However, the change of defect number is quite different in the random alloy and the average atom model. At both temperatures considered here, i.e., 300 and 1000 K, the defect number is higher in the random alloy than in the average atom model. The differences are smaller at the higher temperature of 1000 K.

The above results show that defect accumulation is more efficiently suppressed in the average atom model than in the random alloy at both considered temperatures. This observation is somewhat unexpected since it is well established that the random arrangement of different elements in MPEAs induces variable defect energetics depending on local atomic environments [13,55]. Due to the rough defect energy landscape, defect recombination would be enhanced [14,56,57]. However, these conclusions are obtained by comparing MPEAs (mostly FCC) with their pure constituent elemental metals, which may have distinct defect properties such as formation and migration energies. The present results clearly demonstrate that the effects of the rough energy landscape are limited in enhancing defect recombination in BCC MPEAs when comparing to the average atom model.

Not only are the stable defect numbers different between the random and average alloys, but their defect clustering behaviors are distinct. A visual demonstration of vacancy and interstitial clusters and their distributions in VTaTi is given in Fig. 2 at different temperatures. At 300 K, vacancies are randomly distributed in the system in the form of single vacancies or small clusters. On the other hand, there are almost no individual interstitials in the average model; the interstitials aggregate to $\frac{1}{2}\langle 111 \rangle$ dislocation loops. In contrast, in the random alloy, both interstitial and vacancy defects are discretely distributed. The results hence indicate that fluctuations in the formation and migration energies in the random alloy play a significant role in influencing defect clustering properties in MPEAs.

At a high temperature of 1000 K, defect migration is stimulated. As a result, defect recombination is facilitated by the increased diffusivity of interstitials and vacancies, agreeing with the low defect numbers in Fig. 1. From defect configurations shown in the right column of Fig. 2, it can be seen that fewer defects remain compared to the case of 300 K. In the average atom model, a sizeable interstitial cluster in the form of a $\frac{1}{2}\langle 111 \rangle$ dislocation loop is observed. In contrast, most defects in the random alloy remain isolated; only small interstitial clusters with no more than five defects can be found.

The evolution of vacancy and interstitial clusters in VTaTi at 300 K is further quantified in Fig. 3. In the average atom model, most vacancies are in the form of a single vacancy or small clusters with 2–10 vacancies, even after 4000 FP introduction events. On the other hand, interstitials rapidly aggregated into large clusters containing more than 51 interstitials with increasing FP events, forming $\frac{1}{2}\langle 111 \rangle$ dislocation loops. Hence, it is inferred that interstitial diffusion is efficient for clustering in the average atom model. With increasing FP events, the cluster size first increases and then decreases a little bit, arriving at a saturation state. This is related

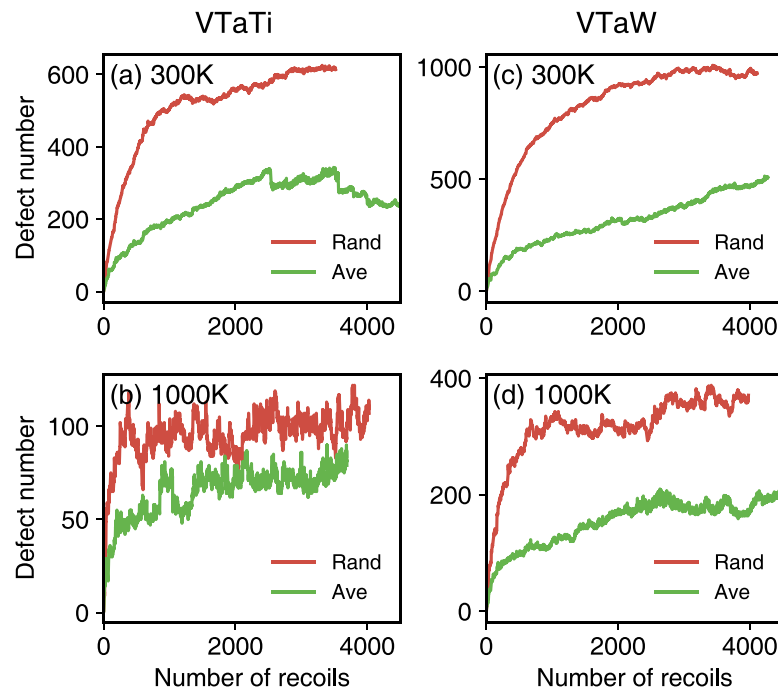


Fig. 1. Defect accumulation in VTaTi and VTaW as a function of the number of FP events. The results obtained in the random alloy and average atom model are shown.

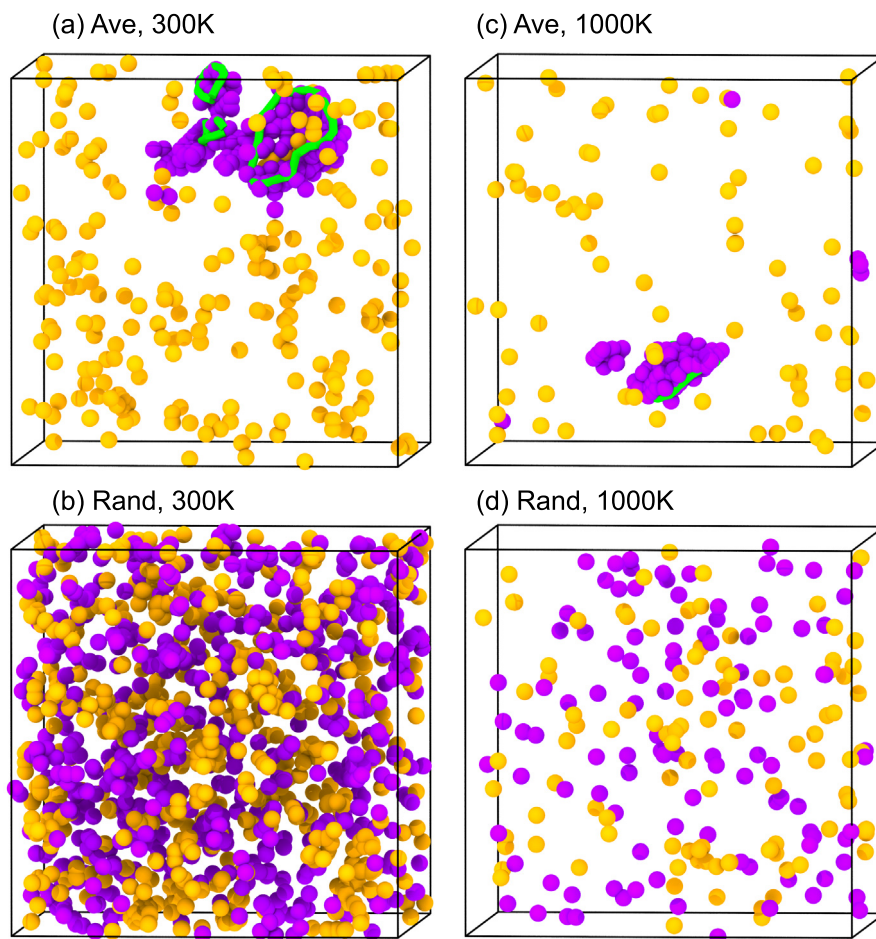


Fig. 2. Defect configurations in VTaTi at the end of the FPA simulations in the average atom model and random alloys. The interstitials are shown in purple, and the vacancies in orange. The green outlines represent dislocation loops.

Table 1

Properties of V calculated by the developed potential. The listed quantities include: lattice constant (a_0), cohesive energies (E_c), vacancy formation energies (E_{fv}), elastic constants (C_{11} , C_{12} , and C_{44}), the bulk modulus (B), structural energy differences between BCC and FCC, simply cubic (SC), and hexagonal closed-packed (HCP) structures ($E_{BCC-FCC}$, $E_{BCC-HCP}$, and E_{BCC-SC}), vacancy migration energy (E_{mv}), surface energy for different orientations ($E_s\{100\}$, $E_s\{110\}$, and $E_s\{111\}$), and the melting temperature (T_m).

	Target values	Present potential	DFT	Previous potential	Exp.
a_0 (Å)	3.03 [51]	3.028	3.000 [48]	3.03 [49], 3.000 [48]	3.03 [51]
E_c (eV/atom)	5.31 [51]	5.31	5.396 [48]	5.31 [49], 5.30 [48]	5.31 [51]
E_{fv} (eV)	2.10 [52]	2.14	2.321 [48]	2.06 [49], 2.376 [48]	2.10 [52]
C_{11} (GPa)	232.40 [53]	232.40	265.0 [48]	232.40 [49], 232.8 [48]	232.40 [53]
C_{12} (GPa)	119.36 [53]	119.36	136.5 [48]	119.36 [49], 121.5 [48]	119.36 [53]
C_{44} (GPa)	45.95 [53]	45.95	30.7 [48]	45.95 [49], 50.1 [48]	45.95 [53]
B (GPa)	157 [53]	157	184.3 [48]	158.5	157 [53]
$E_{BCC-FCC}$ (eV/atom)	-0.16		-0.247 [48]	-0.14 [49], -0.244 [48]	
$E_{BCC-HCP}$ (eV/atom)	-0.16		-0.254 [48]	-0.14 [49], -0.234 [48]	
E_{BCC-SC} (eV/atom)	-0.34			-0.59 [49]	
E_{mv} (eV)	0.57		0.452 [48]	0.51 [49], 0.515 [48]	
$E_s\{100\}$ (J/m ²)	1.90		2.377 [48]	2.605 [48]	
$E_s\{110\}$ (J/m ²)	1.64		2.384 [48]	2.290 [48]	
$E_s\{111\}$ (J/m ²)	2.28		2.681 [48]	2.826 [48]	
T_m (K)	1885			2035 [48]	2183 [54]

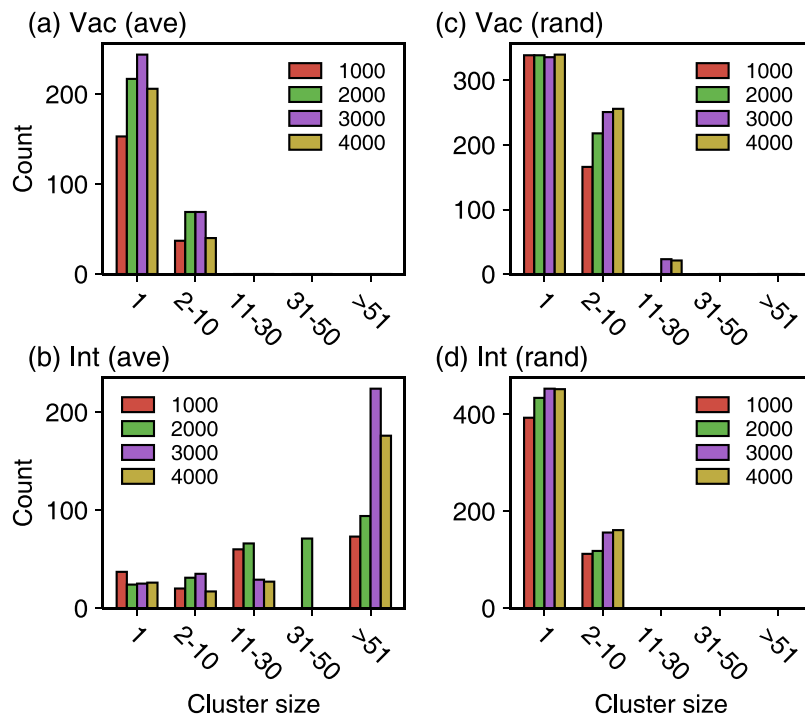


Fig. 3. Cluster size distribution in VTaTi as a function of increasing FP introduction events at 300 K.

to the differences in the mobility of interstitial clusters, as will be discussed below. In the random alloy, the evolution of vacancy and interstitial clusters is nearly the same; only single or small clusters with 2-10 defects are found with increasing FP events. Therefore, clustering through diffusion is highly unlikely in the random alloy. The clustering behavior at 1000 K is similar to the results shown in Fig. 3, in which no large clusters are found in the random alloy.

The above results show that the random MPEA alloy exhibits higher defect numbers compared to the average atom model, but in the form of isolated defects instead of large clusters as in the average atom model. Since the average model bears the averaged defect energetics of the random alloy, the observation suggests that the chemical fluctuations in occupancy and associated lattice distortion can limit the transport of defects. Consequently, recombination of defects is suppressed, resulting in high defect numbers.

For the average atom model, defect recombination is more efficient due to fast defect transport.

The defect clustering behavior in VTaW is similar to that in VTaTi: large interstitial clusters in the form of $\frac{1}{2}\langle 111 \rangle$ dislocations are observed in the average atom model, whereas only discrete defects are found in the random alloy. Nevertheless, it is seen from Fig. 1 that the stable defect number in VTaTi is lower than those in VTaW. In addition, the differences between the average atom model and the random alloy are smaller in VTaTi than in VTaW. These observations are related to the specific defect properties in these two MPEAs.

3.3. Defect properties

To understand the differences in defect accumulation, we calculate defect energetics in VTaTi and VTaW in both the average atom

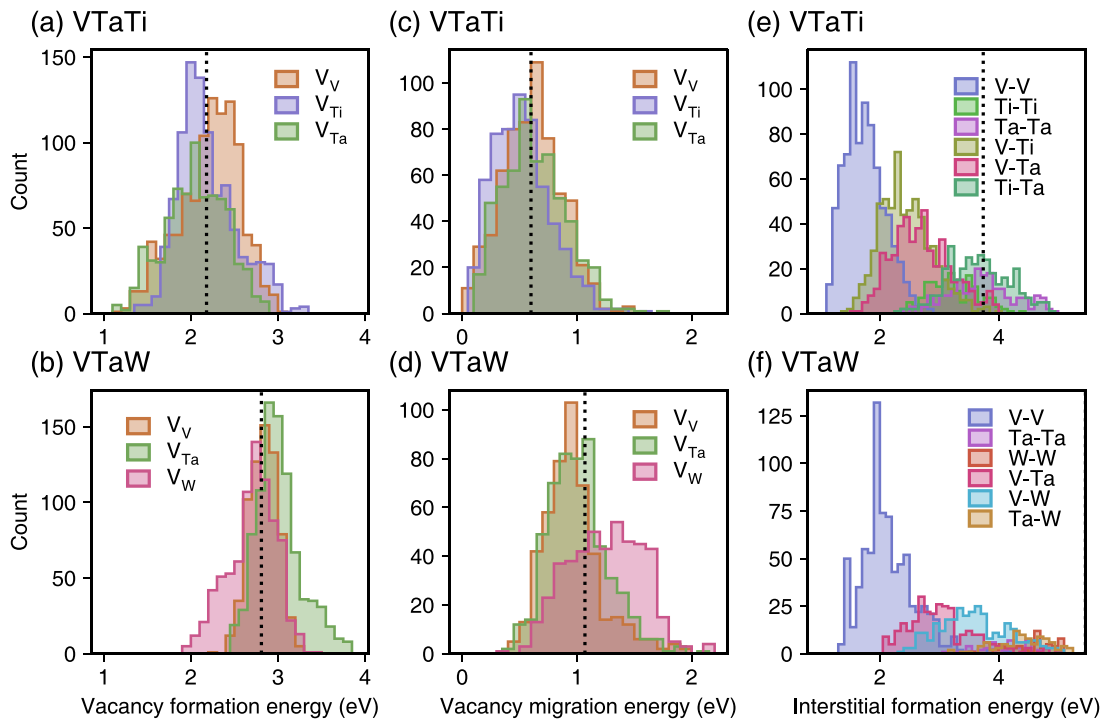


Fig. 4. Comparison of defect energies in VTaTi (first row) and VTaW (second row), including vacancy formation energies, vacancy migration energies, and interstitial formation energies. The dotted lines denote values obtained in the average atom model.

Table 2

Point defect energetics (in eV) in VTaTi and VTaW in the average atom model and the random alloy, including the formation and migration energies for vacancy and interstitial dumbbells with [111] and [110] orientations. The migration energies of interstitials in the average model are calculated through NEB calculations. The migration energies in the random alloy are not shown due to significant interstitial reconstruction, leading it difficult to pre-define a migration path for the interstitial. The migration energies in the last row are obtained from the Arrhenius fitting of the defect diffusivity at different temperatures.

	VTaTi		VTaW	
	Ave	Rand	Ave	Rand
E_f (V)	2.18	2.16	2.81	2.84
E_m (V)	0.60	0.59	1.07	1.07
E_f (I _[111])	3.74	2.57	5.67	2.97
E_f (I _[110])	3.78		5.46	
E_m (I _[111])	0.0003		0.0006	
E_m (I _[110])	0.035		0.217	
E_m (I)	0.002	0.259	0.083	0.204

model and the random alloy. The results are provided in Table 2. In the average atom model, there is only one single value for defect energetics. The energies exhibit distributions in random alloys [55], and we show the distributions in Fig. 4 and their averaged values from all calculated cases (>2000 data points) in Table 2.

Based on the results in Table 2, it is suggested that both vacancies and interstitials have lower formation energies and migration energies in VTaTi than in VTaW. Notably, the migration energies of vacancies and interstitials in VTaTi are almost half of those in VTaW. Therefore, the migration of both vacancies and interstitials is faster in VTaTi. Besides, the difference in the migration energies for vacancy and interstitial, $E_m(V)-E_m(I)$, is considerably lower in VTaTi, an indication of their comparable diffusivities. In the defect accumulation stage, such comparable defect migration may lead to enhanced defect recombination, as observed in Fig. 1, where the overall surviving defect number is lower in VTaTi.

Comparing the obtained energetics in the average atom model and the random alloy, it is found that the formation and migration energies of vacancies are almost identical. However, the formation energies of interstitials are remarkably lower in the random alloy. The lowering of formation energies is attributed to the significant local lattice distortion in the random alloy, as found in previous studies [29]. Because of the distortion, interstitial configurations in the random alloy undergo significant reconstruction depending on local atomic environments. As a result, it is difficult to pre-define a migration path, as in the case of the average atom model, for NEB calculations. In Table 2, the migration energies for interstitials in the random alloy are obtained through the Arrhenius fitting of defect diffusivity at different temperatures, as will be discussed in the next section.

The defect energies in VTaTi and VTaW shown in Fig. 4 exhibit broad distributions. For vacancies, it is found that the distributions of formation and migration energies for each species are largely overlapped in VTaTi. In contrast, the distributions in VTaW are separated. Specifically, W vacancies have low formation energies, and high migration energies relating to vacancy-W exchanges are found. These observations can be partly attributed to the differences in the atomic volume of these species. In VTaTi, the potential predicts comparable volumes for V, Ta, and Ti, which are 16.27, 16.74, and 16.94 Å³/atom, respectively. The atomic volumes are 15.85, 16.21, and 16.13 Å³/atom for V, Ta, and W in VTaW, respectively. The trend of atomic volumes and vacancy formation and migration energetics for these elements is in good agreement with DFT calculations [29]. For example, vacancy-Ta and vacancy-V exchanges possess the lowest barriers in VTaW. For interstitials, V-V dumbbells exhibit the lowest formation energies in both MPEAs, which is consistent with the smallest atomic volume of V.

In the averaged model of VTaTi, the most stable configuration of interstitials is the [111] dumbbell, with a formation energy of 3.74 eV, 0.04 eV lower than that of the [110] dumbbell. On the other hand, in the average model of VTaW, [110] dumbbells exhibit the lowest energy of 5.46 eV, 0.21 eV lower than that of [111]

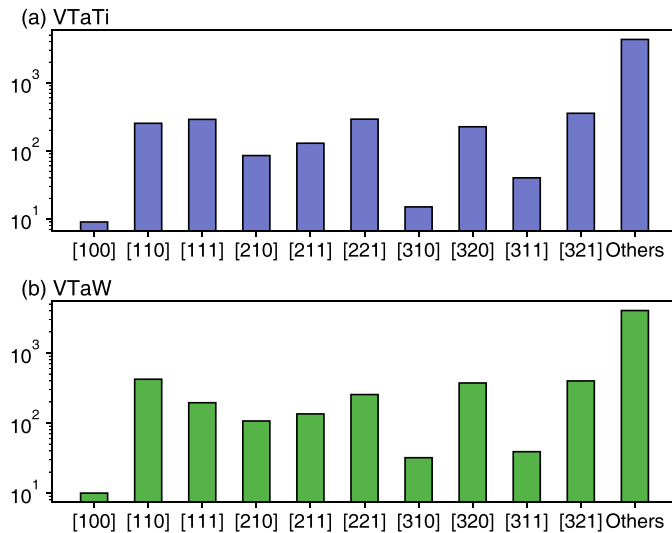


Fig. 5. Orientation of relaxed interstitial dumbbells in the random VTaTi and VTaW alloys. The original orientation of the introduced interstitial is along the [111] direction.

dumbbells. Note that in pure BCC metals, such as V, Ta, and W, the most favorable interstitial dumbbells are along the [110] directions [58]. For Ti with a hexagonal closed-packed (HCP) structure, however, interstitials can occupy various possible interstitial sites, e.g.,

octahedral and tetrahedral sites. This may be a reason leading to the difference in the stability of [110] dumbbells in these two average alloys. In the random alloy, however, interstitial dumbbells may exhibit different orientations depending on local atomic environments. To illustrate this, we show in Fig. 5 the orientations of optimized interstitial configurations in VTaTi and VTaW. The crystalline directions of the axis connecting the two interstitials detected by the WS defect analysis are calculated. We set the tolerance angle for each direction to be 5 °C. For instance, a dumbbell is considered to be along the [100] direction if the angle between the dumbbell axis and one of the six equivalent [100] directions is less than 5 °C. The results clearly show that interstitial dumbbells exhibit a variety of orientations other than the high-symmetric ones, such as [110], [111], and [221] directions. Therefore, the fluctuations in chemical occupancy and lattice distortion make interstitials in MPEAs exhibit anisotropic properties. Besides, it leads to lower formation energies for interstitials, as compared to the average atom model. The decrease of formation energies is more pronounced in VTaW than in VTaTi, in accordance with the larger local lattice distortion of VTaW.

In BCC metals, it is well established that the migration of [111] dumbbells proceeds through fast translation along the [111] direction. This is in accordance with our NEB calculations, which show that the energy barrier is almost zero (Table 2) in the average atom model. For the rotation and translation migration of [110] dumbbell in the average atom model, the barriers are found to be 0.04 and 0.22 eV in VTaTa and VTaW, respectively. These results suggest fast

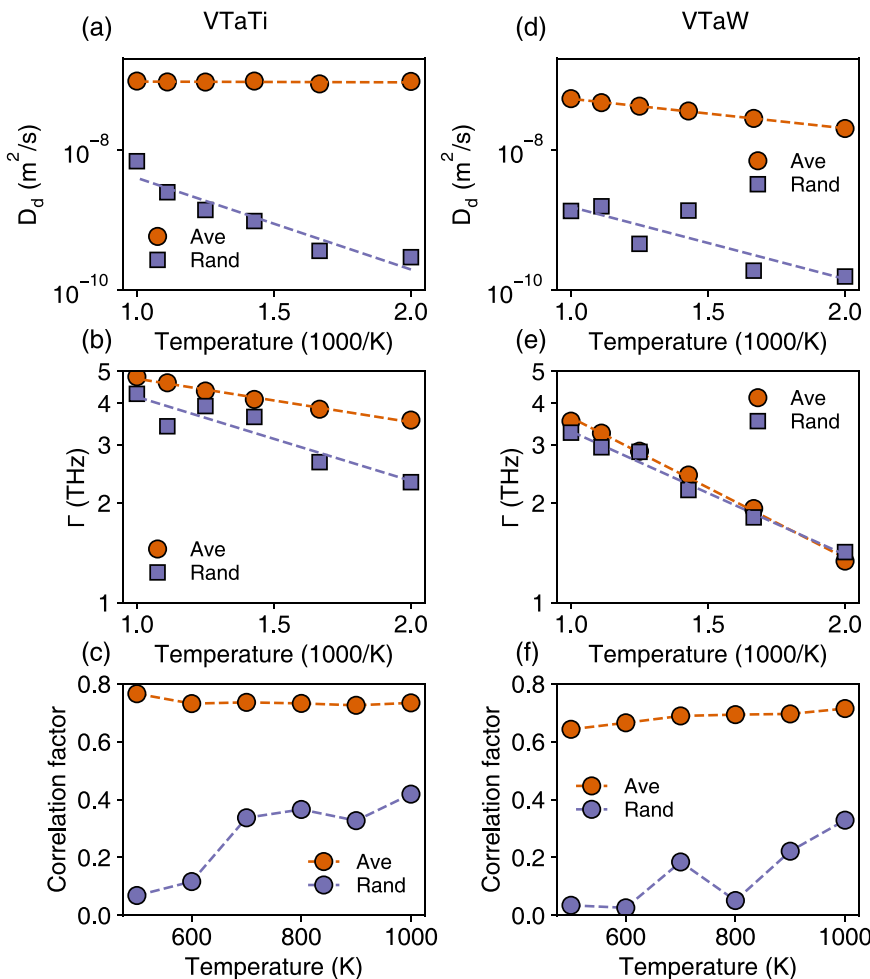


Fig. 6. Comparison of diffusion properties of single interstitial in VTaTi and VTaW. (a) and (d) shows the defect diffusivity, (c) and (e) show the jump frequency, (c) and (f) the correlation factor.

transport of interstitials is expected in the average atom model. In random alloys, due to the versatile interstitial orientations displayed in Fig. 5, there may be several mechanisms for interstitial migration operative simultaneously. To gain an overall picture of interstitial diffusion, we carry out MD at different temperatures.

3.4. Diffusion mechanism

To understand the observed behavior of defect accumulation and defect evolution, we study the diffusion of a single interstitial and its clusters through MD at different temperatures. The diffusion properties of single interstitial in VTaTi and VTaW, including the defect diffusivity D_d , jump frequency Γ , and correlation factor f_c , are compared in Fig. 6. It is shown that the diffusivity of interstitial is strongly suppressed in the random alloy compared to the average atom model. This observation provides evidence that local fluctuations in chemical occupancy and accompanying defect energy fluctuations play decisive roles in governing diffusion properties. The differences in D_d are more pronounced in VTaTi than in VTaW. D_d is related to the jump frequency and the correlation factor through Eq. (3). The jump frequency and correlation factor shown in Fig. 6 indicate that the main differences between these two MPEA come from the jump frequency.

In the average atom model, we find interstitials may be in the form of either [110] or [111] dumbbells during diffusion. The migration of [111] dumbbells proceeds through fast translation along the [111] direction, while the [110] dumbbells migration involves a translation and rotation process. As a result, single interstitial diffuses through three-dimensional (3D) motion in the whole system, the trajectory of which is displayed in Fig. 7. Such 3D diffusion mode can facilitate recombination between Frenkel pairs, since the fast-moving interstitial can move around and lead to recombination with vacancies in its trajectory. In contrast, in the random alloy, there are strong pinning points for the interstitial, leading to retarded diffusion. Such pinning effects can be attributed to the energy distributions in Fig. 4, which shows that the interstitial may exhibit relatively low formation energies. The interstitial is quite stable at these low-energy configurations, and it spends a long time in these states before it can jump out. Consequently, the trajectory of the interstitial is rather localized in this case, which can only lead to recombination with nearby vacancies. This is the reason why the average atom model exhibits a lower defect number compared to the random alloy, as shown in Fig. 1. Moreover, in the random alloy, the retarded diffusion explains most interstitials are in the form of single interstitial or small clusters with 2–10 interstitials, while interstitials rapidly aggregated into large clusters in the average model (Fig. 3).

The trap of the interstitial in the random alloy results in a significant decrease of jump frequency since the low-energy configurations are quite stable. Comparing VTaTi and VTaW, it is found that the distribution of interstitial formation energies is broader in VTaTi than in VTaW, which is in accordance with the more significant decrease of jump frequency in the random VTaTi compared to the average model. In addition to the change of jump frequency, diffusion of interstitial in the random alloy is highly correlated (Fig. 6), especially at low temperatures, as expected from the energy distributions. If the defect jumps over a low energy barrier, it is highly likely that the defect can jump back and leads to correlation effects. However, in the average model, all defect jump directions are equally probable without significant correlations. Both the decrease of jump frequencies and the correlation factors contribute to the low diffusivity of single interstitials in the random alloys.

Owing to the higher diffusivity of interstitials over vacancies, the diffusion of a single interstitial and its clusters plays a major role in determining defect evolution. We further simulate the dif-

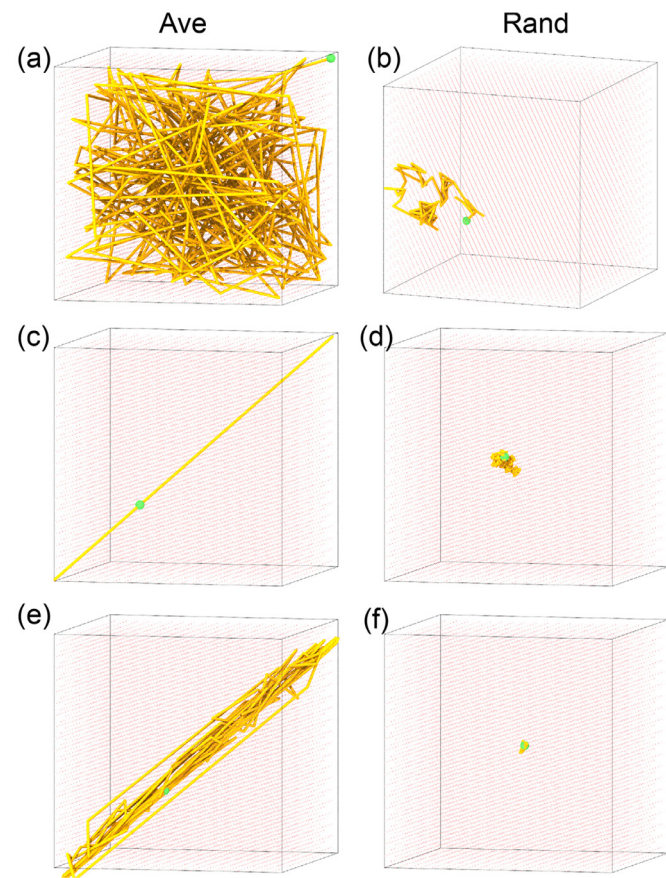


Fig. 7. Comparison of trajectories of interstitials in VTaTi in the average atom model and the random alloy at 600 K. Three different interstitial sizes are shown, I_1 in (a) and (b), I_{10} in (c) and (d), and I_{25} in (e) and (f).

fusion of interstitial clusters with different sizes containing 2 to 25 interstitials. The trajectories of selective interstitial clusters (I_1 , I_{10} , and I_{25}) simulated at 600 K in VTaTi are provided in Fig. 7. In the average atom model, the migration mode changes from 3D motion to 1D motion along the [111] direction with the increase of interstitial size. Nevertheless, in the random alloy, interstitial clusters tend to be trapped in the local environment throughout almost the whole simulation. This trapping effect is more prominent for large interstitial clusters, suggesting strong pinning effects.

The jump frequency for interstitial clusters with different sizes at different temperatures is shown in Fig. 8 for VTaTi. It is suggested that the jump frequency for every interstitial cluster in the average atom model follows the Arrhenius relation in Eq. (4) nicely. The jump frequency decreases with increasing interstitial sizes, as expected. On the other hand, in the random alloy, the temperature dependence of jump frequency cannot be adequately described by an Arrhenius relation. Due to the above-discussed local trapping effects, it is difficult for the interstitial cluster to migrate over a distance larger than the 1nn distance. In most of the simulation time, the interstitial cluster just rearranges itself without long-range diffusion. As a consequence, the jump frequency strongly depends on the atomic element distributions presented in the nearby region surrounding the interstitial cluster. Besides, the jump frequency is significantly lower in the random alloy than in the average model.

These observations can be ascribed to the fluctuations in defect energies, which provide substantial low-energy valleys where the interstitials are stable and difficult to jump to high-energy configurations. The formation energies of the considered interstitial clus-

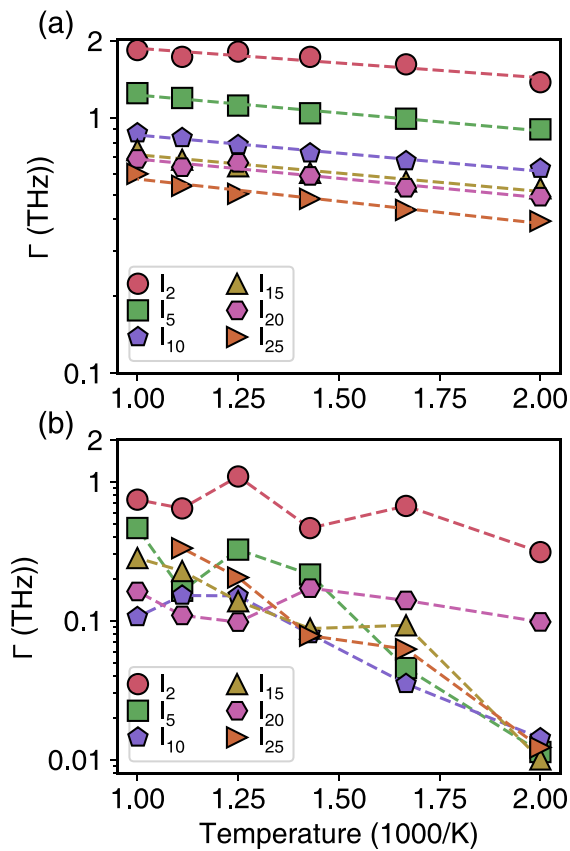


Fig. 8. Jump frequency of interstitial clusters with different sizes at different temperatures in VTaTi. (a) shows the results in the average atom model, and (b) shows the results in the random VTaTi.

ters are provided in Fig. 9. The formation energies exhibit broad distributions in the random alloys, whereas there is only one formation energy in the averaged atom model. As interstitials favor low energy states, the energy distributions suggest that there are considerable low energy trap sites for interstitials. As long as interstitials are located at these states, the chances are that they will stay at the same position for a long time, since the energy barriers for them to escape from these sites are high. On the other hand, interstitials can move freely in the average atom model through 1D motion. As large interstitial clusters can fast diffuse through 1D mode, they can recombine with surrounding vacancies, leading to a saturated cluster size distribution as shown in Fig. 3.

Due to the large size mismatch in BCC MPEAs, interstitials composed of elements with small atomic sizes are favorable. In the considered MPEAs, V has the smallest atomic size. Consequently, interstitial diffusion is mediated mainly by the V elements. Inspection of the interstitial configurations during our MD trajectories suggests that almost all the interstitial diffusion involves V, dictating strongly chemically biased diffusion [39,59]. We have further checked the influence of atomic compositions in the surroundings of the interstitial clusters on their formation energies. The results suggest that the interstitial clusters exhibit lower energies when they are surrounded by more V atoms. An example for I_{10} is displayed in the Appendix (Fig. 10). Therefore, it is envisaged that segregation of V elements is expected around interstitial clusters. Since chemically-biased diffusion in the MPEA is mediated through V, and the interstitial clusters tend to be surrounded by V, a presence of V-rich second-phase particles may act as a strong pinning point for defect clusters, as reported in the experiment [17].

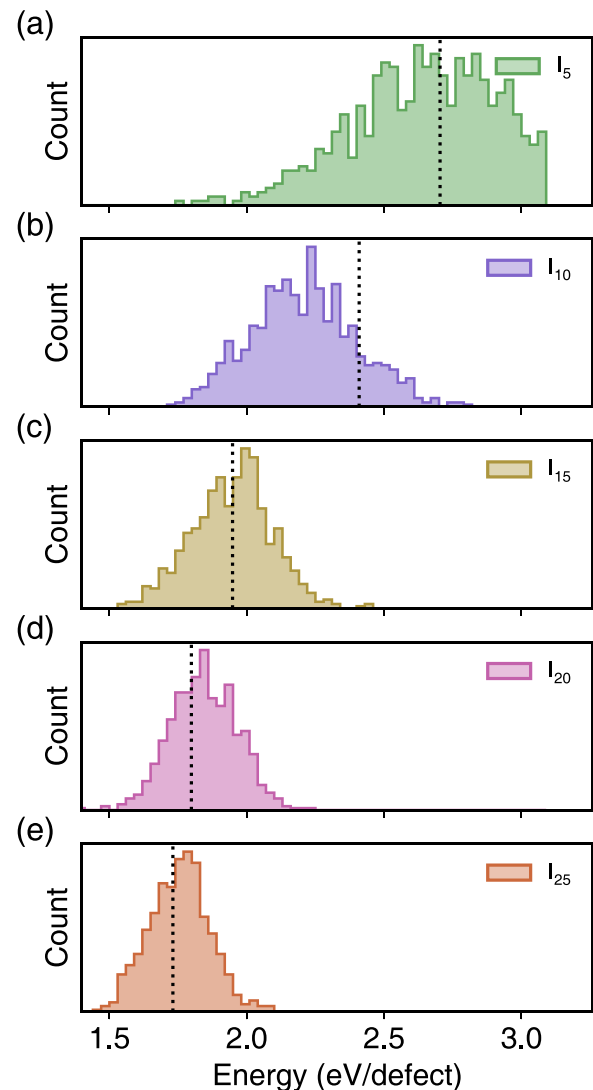


Fig. 9. Distribution of formation energies of interstitial clusters in VTaTi. The dotted line in each graph shows the results obtained in the average atom model.

4. Discussion

By comparing defect evolution in the true random alloy and the average atom model, we can isolate the effects of chemical fluctuations on the irradiation response of MPEAs. In general, the average atom model represents the average properties of the random alloy, including bulk modulus, defect energies, etc., but without local fluctuations. Therefore, such a comparison is ideal for revealing the role of chemical complexity, elucidating how local fluctuations in defect energies can affect defect evolution. Note that most previous studies focus on comparing random alloy with pure metals derived from its composition. For instance, the irradiation resistance of Ni-containing concentrated alloys is compared to pure Ni to illustrate the effects of the chemical disorder [14,60–62]. Since their atomic compositions, concentrations, and material properties (defect energetics) are all different, such comparisons may complicate the analysis of chemical complexity peculiar to MPEAs.

Our results indicate that the chemical fluctuations are critical factors influencing defect evolution in refractory MPEAs. Through FPA simulations, we reveal that the fluctuations have adverse effects on defect recombination. Specifically, in the random alloy, defect motion is suppressed since the defect energy landscape is very

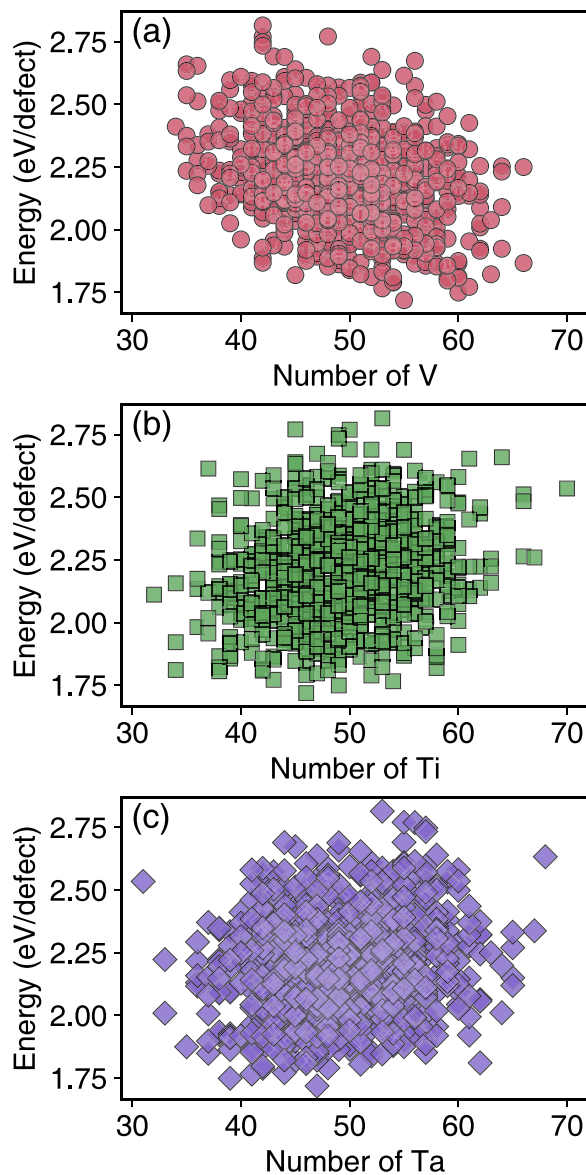


Fig. 10. Dependence of the formation energy of I_{10} interstitial clusters on the surrounding atomic environments as quantified by the number of different elements within its 5 Å radius.

rough, especially for interstitials. As a result, interstitials can only move around in a localized region, as verified by our MD simulations. On the other hand, interstitials in the average atom model can migrate through either 3D (single interstitial) or 1D (interstitial clusters), facilitating defect recombination and leading to overall lower defect numbers. The differences in diffusion further lead to large cluster formation in the average atom model, whereas only discrete defect clusters are found in the random alloy. These results thus suggest that the dominant role of chemical fluctuations is on the defect forms under irradiation; it leads to discrete, small-scale defects. This is in good agreement with experimental observations that only small defects are found in BCC MPEAs [20,30,31].

Almost all previous computational studies on the irradiation response of MPEAs are concentrated on FCC ones [12,13,44,46,47,63,64]. Different from FCC MPEAs, BCC ones usually exhibit significant local lattice distortions, which have profound influences on defect energetics [29]. The most prominent feature is the low interstitial formation energies due to local relaxation. As shown in Fig. 4, there is a sizable portion of interstitial forma-

tion energies lower than 1 eV, even lower than those of vacancies. Besides, interstitials may be stabilized in different orientations (Fig. 5). These are all absent in FCC MPEAs. For instance, in FCC NiCoCr and NiCoFeCr, all the formation energies of interstitials from DFT calculations are higher than those of vacancies [13]. The consequence of such low-energy interstitial configurations is that interstitials may be trapped in these low-energy valleys. In FCC MPEAs, it is argued that interstitials in FeNi migrate through 3D motion, whereas in pure Ni, migration proceeds through 1D motion [9]. In contrast, our results show that in BCC MPEAs, the interstitials can just be trapped in a local atomic environment without long-range diffusion. Therefore, interstitial movement is essentially frozen in BCC MPEAs, especially for moderate to large interstitial clusters.

Generally, the irradiation mechanism in materials can be described by a ballistic collision stage and kinetic relaxation stage [23]. In the ballistic stage, Frenkel defects are created due to collision cascade; those defects evolve, undergo either recombine or clustering in the kinetic stage. By directly simulating Frenkel pair accumulation instead of collision cascade, the mechanism of defect evolution can be captured, and significant insight into the radiation response of materials can be gained. In MPEAs, it has been realized that the improved irradiation tolerance cannot be ascribed to the ballistic stage but more dependent on the relaxation stage [14,65]. A very recent publication [66] further substantiates this conclusion based on cascade collision simulations in a random FCC MPEA and the average atom model. Therefore, in this work, we focus on the relaxation stage to reveal the effects of chemical disorder on the irradiation response of MPEAs. Our results demonstrate that chemical disorder indeed affects defect evolution merely due to the randomness of elemental arrangement and associated lattice distortion, which is the most basic characteristic of MPEAs. Even if we have a model alloy with all the averaged properties of the MPEA, the inherent chemical disorder can strongly affect the mechanism of defect motion, hence influence defect evolution.

5. Conclusion

We have compared defect evolution properties in two BCC MPEAs with their average atom models. For this purpose, we have parameterized the EAM potential for V metal with a good agreement with materials values. Comparison between the random alloy and the average atom potential helps us reveal the effects of chemical fluctuations on defect evolution. Our results show that the fluctuations in chemical occupancy and associated local lattice distortion play significant roles in defect accumulation and defect diffusion. Particularly, fluctuations-induced defect energy distributions lead to a rough defect energy landscape, which can trap interstitial motion. As a consequence, defect recombination can only occur in a local region, leading to discrete defect distribution in random MPEAs. These results highlight the importance of chemical fluctuations in influencing the irradiation response of BCC MPEAs and providing a sensible way to tune and improve irradiation resistance of refractory MPEAs by modulating chemical fluctuations. This work, together with previous results on collision cascade in random and average MPEAs [66], affirms that the origin of the experimentally observed irradiation tolerance of MPEAs is not from primary damage but from long-term defect evolution due to disorder-modified defect migration mechanisms.

Declaration of Competing Interest

The authors declare that they have no known competing financial interests or personal relationships that could have appeared to influence the work reported in this paper.

Acknowledgment

This work was supported by National Natural Science Foundation of China (No. 11975193), City University of Hong Kong (No. 9610425), Research Grant Council of Hong Kong (No. 21200919), Guangdong Basic and Applied Basic Research Foundation (Nos. 2019A1515011528 and 2021A1515010545), and Shenzhen Basic Research Program (No. JCYJ20190808181601662). This work was carried out using the computational facilities, CityU Burgundy, managed and provided by the Computing Services Centre at City University of Hong Kong.

Appendix

The fitted potential parameters for pure V metal are listed in **Table 3**. For completeness, we reproduce the EAM formalism used

Table 3
EAM potential parameters for V. The symbols are the same as in the original formalism as stated in [34].

r_e	2.594662
f_e	2.523567
α	7.515860
β	4.908879
A	0.631438
B	0.886485
κ	0.185170
λ	0.419307
ρ_e	27.724393
ρ_s	27.724393
F_{ni} ($i=0,1,2,3$)	-3.352734, -0.254664, 0.640819, -2.830487
F_i ($i=0,1,2,3$)	-3.380243, 0, 1.242722, 0.134111, 0.000000
η	0.635059
F_e	-3.365898

in this potential [34] as follows.

The total energy is given by:

$$E = \frac{1}{2} \sum_{i,j,i \neq j} \phi_{ij}(r_{ij}) + \sum_i F_i(\rho_i), \quad (6)$$

where ϕ_{ij} is the pair energy between atoms i and j at a distance of r_{ij} , and F_i is the embedding energy associated with embedding an atom i into a local site with an electron density $\rho_i = \sum_{j,j \neq i} f_j(r_{ij})$.

The generalized elemental pair potentials are defined as

$$\phi_{ij}(r) = \frac{A \exp[-\alpha(r/r_e - 1)]}{1 + (r/r_e - \kappa)^{20}} - \frac{B \exp[-\beta(r/r_e - 1)]}{1 + (r/r_e - \lambda)^{20}}, \quad (7)$$

where r_e is the equilibrium distance between nearest neighbors, A , B , α , and β are four tunable parameters, and λ and κ are two additional parameters for the cutoff.

The electron density function is taken with the same form as the attractive term in the pair potential with the same values of β and λ :

$$f(r) = \frac{f_e \exp[-\beta(r/r_e - 1)]}{1 + (r/r_e - \lambda)^{20}} \quad (8)$$

Table 4

Properties of VTaTi and VTaW calculated with average atom potential and the true random alloy potential. The lattice constants are comparable with previous DFT and experiments.

	VTaTi			VTaW		
	Average potential	Alloy potential	literature	Average potential	Alloy potential	literature
a_0 (Å)	3.221	3.217	3.20 [50]/3.208[32]	3.180	3.179	3.17[50]
C_{11} (GPa)	185	185		306	301	
C_{12} (GPa)	121	122		139	142	
C_{44} (GPa)	69	64		89	81	
B (GPa)	142	143		194	195	

- [11] Y.-J. Liang, L. Wang, Y. Wen, B. Cheng, Q. Wu, T. Cao, Q. Xiao, Y. Xue, G. Sha, Y. Wang, Y. Ren, X. Li, L. Wang, F. Wang, H. Cai, High-content ductile coherent nanoprecipitates achieve ultrastrong high-entropy alloys, *Nat. Commun.* 9 (2018) 4063.
- [12] Y. Zhang, S. Zhao, W.J. Weber, K. Nordlund, F. Granberg, F. Djurabekova, F. Granberg, F. Djurabekova, Atomic-level heterogeneity and defect dynamics in concentrated solid-solution alloys, *Curr. Opin. Solid State Mater. Sci.* 21 (2017) 221–237.
- [13] S. Zhao, Y. Zhang, W.J. Weber, High entropy alloys: irradiation, *Ref. Modul. Mater. Sci. Mater. Eng.* (2020) Elsevier, doi:10.1016/B978-0-12-803581-8.11713-8.
- [14] T. Yang, C. Li, S.J. Zinkle, S. Zhao, H. Bei, Y. Zhang, Irradiation responses and defect behavior of single-phase concentrated solid solution alloys, *J. Mater. Res.* 33 (2018) 3077–3091.
- [15] N.A.P.K. Kumar, C. Li, K.J. Leonard, H. Bei, S.J. Zinkle, Microstructural stability and mechanical behavior of FeNiMnCr high entropy alloy under ion irradiation, *Acta Mater.* 113 (2016) 230–244.
- [16] C. Li, X. Hu, T. Yang, N.L. Kumar, B.D. Wirth, S.J. Zinkle, Neutron irradiation response of a Co-free high entropy alloy, *J. Nucl. Mater.* 527 (2019) 151838.
- [17] O. El-Atwani, N. Li, M. Li, A. Devaraj, J.K.S. Baldwin, M.M. Schneider, D. Sobieraj, J.S. Wróbel, D. Nguyen-Manh, S.A. Maloy, E. Martinez, Outstanding radiation resistance of tungsten-based high-entropy alloys, *Sci. Adv.* 5 (2019) eaav2002.
- [18] P.J. Barron, A.W. Carruthers, J.W. Fellowes, N.G. Jones, H. Dawson, E.J. Pickering, Towards V-based high-entropy alloys for nuclear fusion applications, *Scr. Mater.* 176 (2020) 12–16.
- [19] Z. Sun, H. Cui, Microstructure and mechanical properties of low-activation Fe-Cr-V multicomponent single-phase alloys, *J. Mater. Eng. Perform.* 27 (2018) 3394–3400.
- [20] M. Sadeghilaridjani, A. Ayyagari, S. Muskeri, V. Hasannaeimi, R. Salloom, W.Y. Chen, S. Mukherjee, Ion irradiation response and mechanical behavior of reduced activity high entropy alloy, *J. Nucl. Mater.* 529 (2020) 151955.
- [21] S.J. Zinkle,R.J.M. Konings, R.E. Stoller (Eds.), Radiation-induced effects on microstructure, *Compr. Nucl. Mater.* (2012) 65–98.
- [22] G.S. Was, *Fundamentals of Radiation Materials Science: Metals and Alloys*, Springer Science & Business Media, 2007.
- [23] R.E. Stoller, Primary radiation damage formation, in: R.J.M. Konings, R.E. Stoller (Eds.), *Compr. Nucl. Mater.*, Elsevier, 2012, pp. 293–332.
- [24] S. Zhao, W.J. Weber, Y. Zhang, Unique Challenges for Modeling Defect Dynamics in Concentrated Solid-Solution Alloys, *Jom* 69 (2017) 2084–2091.
- [25] S. Zhao, Y.N. Osetsky, Y. Zhang, Atomic-scale dynamics of edge dislocations in Ni and concentrated solid solution NiFe alloys, *J. Alloys Compd.* 701 (2017) 1003–1008.
- [26] Y. Tong, S. Zhao, H. Bei, T. Egami, Y. Zhang, F. Zhang, Severe local lattice distortion in Zr- and/or Hf-containing refractory multi-principal element alloys, *Acta Mater.* 183 (2020) 172–181.
- [27] R. Huang, Q. Zhang, X. Zhang, J. Li, T. Cao, J. Yao, Y. Xue, H. Gao, X. Li, Dynamic recrystallization-induced temperature insensitivity of yield stress in single-crystal Al1.2CrFeCoNi micropillars, *Sci. China Technol. Sci.* 64 (2021) 11–22.
- [28] Q. Zhang, R. Huang, X. Zhang, T. Cao, Y. Xue, X. Li, Deformation mechanisms and remarkable strain hardening in single-crystalline high-entropy-alloy micropillars/nanopillars, *Nano Lett.* 21 (2021) 3671–3679.
- [29] S. Zhao, Defect properties in a VTaCrW equiatomic high entropy alloy (HEA) with the body centered cubic (bcc) structure, *J. Mater. Sci. Technol.* 44 (2020) 133–139.
- [30] A. Kareer, J.C. Waite, B. Li, A. Couet, D.E.J. Armstrong, A.J. Wilkinson, Short communication: 'Low activation, refractory, high entropy alloys for nuclear applications, *J. Nucl. Mater.* 526 (2019) 151744.
- [31] C. Parkin, M. Moorehead, M. Elbakhshwan, J. Hu, W.-Y. Chen, M. Li, L. He, K. Sridharan, A. Couet, In situ microstructural evolution in face-centered and body-centered cubic complex concentrated solid-solution alloys under heavy ion irradiation, *Acta Mater.* 198 (2020) 85–99.
- [32] N. Jia, Y. Li, X. Liu, Y. Zheng, B. Wang, J. Wang, Y. Xue, K. Jin, Thermal Stability and Mechanical Properties of Low-Activation Single-Phase Ti-V-Ta Medium Entropy Alloys, *Jom.* 71 (2019) 3490–3498.
- [33] S. Plimpton, Fast parallel algorithms for short-range molecular dynamics, *J. Comput. Phys.* 117 (1995) 1–19.
- [34] X.W. Zhou, R.A. Johnson, H.N.G. Wadley, Misfit-energy-increasing dislocations in vapor-deposited CoFe/NiFe multilayers, *Phys. Rev. B.* 69 (2004) 144113.
- [35] C. Varvenne, A. Luque, W.G. Nöhring, W.A. Curtin, Average-atom interatomic potential for random alloys, *Phys. Rev. B.* 93 (2016) 104201.
- [36] A. Chartier, M.-C. Marinica, Rearrangement of interstitial defects in alpha-Fe under extreme condition, *Acta Mater.* 180 (2019) 141–148.
- [37] A. Stukowski, Visualization and analysis of atomistic simulation data with OVITO-the Open Visualization Tool, *Model. Simul. Mater. Sci. Eng.* 18 (2010) 15012.
- [38] G. Henkelman, B.P. Uberuaga, H. Jónsson, Climbing image nudged elastic band method for finding saddle points and minimum energy paths, *J. Chem. Phys.* 113 (2000) 9901–9904.
- [39] S. Zhao, Y. Osetsky, Y. Zhang, Preferential diffusion in concentrated solid solution alloys: NiFe, NiCo and NiCoCr, *Acta Mater.* 128 (2017) 391–399.
- [40] Y.N. Osetsky, D.J. Bacon, A. Serra, B.N. Singh, S.I. Golubov, One-dimensional atomic transport by clusters of self-interstitial atoms in iron and copper, *Philos. Mag.* 83 (2003) 61–91.
- [41] N. Anento, A. Serra, Y.N. Osetsky, Atomistic study of multimechanism diffusion by self-interstitial defects in α -Fe, *Model. Simul. Mater. Sci. Eng.* 18 (2010) 25008.
- [42] S. Zhao, Y. Osetsky, Y. Zhang, Diffusion of point defects in ordered and disordered Ni-Fe alloys, *J. Alloys Compd.* 805 (2019) 1175–1183.
- [43] Y.N. Osetsky, Atomistic study of diffusional mass transport in metals, *Diffus. Defect Data. Pt A Defect Diffus. Forum* (2001) 71–92.
- [44] L. Koch, F. Granberg, T. Brink, D. Utt, K. Albe, F. Djurabekova, K. Nordlund, Local segregation versus irradiation effects in high-entropy alloys: steady-state conditions in a driven system, *J. Appl. Phys.* 122 (2017) 105106.
- [45] F. Granberg, J. Byggmästar, K. Nordlund, Defect accumulation and evolution during prolonged irradiation of Fe and FeCr alloys, *J. Nucl. Mater.* 528 (2020) 151843.
- [46] L.K. Béland, C. Lu, Y.N. Osetskiy, G.D. Samolyuk, A. Caro, L. Wang, R.E. Stoller, Features of primary damage by high energy displacement cascades in concentrated Ni-based alloys, *J. Appl. Phys.* 119 (2016) 085901.
- [47] E. Levo, F. Granberg, C. Fridlund, K. Nordlund, F. Djurabekova, Radiation damage buildup and dislocation evolution in Ni and equiatomic multicomponent Ni-based alloys, *J. Nucl. Mater.* 490 (2017) 323–332.
- [48] S.B. Maisel, W.S. Ko, J.L. Zhang, B. Grabowski, J. Neugebauer, Thermomechanical response of NiTi shape-memory nanoprecipitates in TiV alloys, *Phys. Rev. Mater.* 1 (2017) 33610.
- [49] P.A.T. Olsson, Semi-empirical atomistic study of point defect properties in BCC transition metals, *Comput. Mater. Sci.* 47 (2009) 135–145.
- [50] S. Zhao, Local Ordering Tendency in Body-Centred Cubic (BCC) Multi-Principal Element Alloys, *J. Phase Equilibria Diffus.* (2021), doi:10.1007/s11669-021-00878-w.
- [51] C. Kittel, D.F. Holcomb, *Introduction to Solid State Physics*, Wiley, 1967.
- [52] R.A. Johnson, D.J. Oh, Analytic embedded atom method model for bcc metals, *J. Mater. Res.* 4 (1989) 1195–1201.
- [53] G. Simmons, *Single Crystal Elastic Constants and Calculated Aggregate Properties*, Southern Methodist Univ Dallas Tex., 1965.
- [54] A.T. Dinsdale, SGTE data for pure elements, *Calphad* 15 (1991) 317–425.
- [55] S. Zhao, G.M. Stocks, Y. Zhang, Defect energetics of concentrated solid-solution alloys from ab initio calculations: $\text{Ni}_{0.5}\text{Co}_{0.5}$, $\text{Ni}_{0.5}\text{Fe}_{0.5}$, $\text{Ni}_{0.8}\text{Fe}_{0.2}$ and $\text{Ni}_{0.8}\text{Cr}_{0.2}$, *Phys. Chem. Chem. Phys.* 18 (2016) 24043–24056.
- [56] S. Zhao, Y. Osetsky, A.V. Barashev, Y. Zhang, Frenkel defect recombination in Ni and Ni-containing concentrated solid-solution alloys, *Acta Mater.* 173 (2019) 184–194.
- [57] Y. Zhang, K. Jin, H. Xue, C. Lu, R.J. Olsen, L.K. Béland, M.W. Ullah, S. Zhao, H. Bei, D.S. Aidhy, G.D. Samolyuk, L. Wang, M. Caro, A. Caro, G.M. Stocks, B.C. Larson, I.M. Robertson, A.A. Correa, W.J. Weber, Influence of chemical disorder on energy dissipation and defect evolution in advanced alloys, *J. Mater. Res.* 31 (2016) 2363–2375.
- [58] D. Nguyen-Manh, A.P. Horsfield, S.L. Dudarev, Self-interstitial atom defects in bcc transition metals: group-specific trends, *Phys. Rev. B - Condens. Matter Mater. Phys.* 73 (2006) 020101.
- [59] Y.N. Osetsky, L.K. Béland, R.E. Stoller, Specific features of defect and mass transport in concentrated fcc alloys, *Acta Mater.* 115 (2016) 364–371.
- [60] M.W. Ullah, D.S. Aidhy, Y. Zhang, W.J. Weber, Damage accumulation in ion-irradiated Ni-based concentrated solid-solution alloys, *Acta Mater.* 109 (2016) 17–22.
- [61] G. Veliš, E. Wendler, S. Zhao, K. Jin, H. Bei, W.J. Weber, Y. Zhang, Delayed damage accumulation by athermal suppression of defect production in concentrated solid solution alloys, *Mater. Res. Lett.* 6 (2018) 136–141.
- [62] M.W. Ullah, H. Xue, G. Veliš, K. Jin, H. Bei, W.J. Weber, Y. Zhang, Effects of chemical alternation on damage accumulation in concentrated solid-solution alloys, *Sci. Rep.* 7 (2017) 4146.
- [63] S. Zhao, On the role of heterogeneity in concentrated solid-solution alloys in enhancing their irradiation resistance, *J. Mater. Res.* 35 (2020) 1103–1112.
- [64] M.A. Cusentino, M.A. Wood, R. Dingreville, Compositional and structural origins of radiation damage mitigation in high-entropy alloys, *J. Appl. Phys.* 128 (2020) 125904.
- [65] S. Zhao, B. Liu, G.D. Samolyuk, Y. Zhang, W.J. Weber, Alloying effects on low-energy recoil events in concentrated solid-solution alloys, *J. Nucl. Mater.* 529 (2020) 151941.
- [66] O.R. Deluigi, R.C. Pasianot, F.J. Valencia, A. Caro, D. Farkas, E.M. Bringa, Simulations of primary damage in a High Entropy Alloy: probing enhanced radiation resistance, *Acta Mater.* 213 (2021) 116951.